Check for updates

Enhanced electrochemical dissolution of iridium oxide in acidic electrolytes through presence of metal ions: shortened lifetime and hope for recovery

Raghunandan Sharma, [ID] *[a] Per Morgen,[a] Darko Makovec, [ID] [b] Saso Gyergyek [ID] [b] and Shuang Ma Andersen [ID] *[a]

Nanoparticulate Ir-oxides are frequently used as highly active and robust anode electrocatalysts for acidic water electrolyzers. While their dissolution during the electrolyzer operation is unsought, it could be a green route for recovery of Ir from the spent electrodes. In this study, we explore such a possibility and show that the electrochemical dissolution of Ir-oxides during a potential cycling treatment can be enhanced by introducing transition metal ions (such as Cu^{2+}) in the acidic electrolyte. Dissolution of Ir from a nanoparticulate Ir-oxide containing electrode through potential cycling between 0.0 and 1.65 V in 1 M HCl increases by a factor of $\sim$3 in the presence of low concentrations (*e.g.* 10 mM) of Cu^{2+}. Impact of the presence of the metal ions on the Ir-oxide dissolution mechanism is characterized. Cyclic deposition and stripping of the Cu^{2+} ion on the Ir-oxide may be attributed to the enhanced Ir dissolution, as evidenced by cyclic voltammograms studied in detail for Cu^{2+}. Apart from exploration of the possibility of the electrochemical dissolution-based recovery of Ir from the spent Ir-oxide electrocatalysts, the study highlights the generally negative impacts of the presence of certain metal ions in the feedstock water on the electrocatalyst durability in acidic water electrolysis. Outcomes of this study are highly relevant for the fast-growing acidic water electrolysis industry.

Sustainability spotlight

Green hydrogen production based on water electrolysis is adopted by many advanced nations. A key bottleneck for the PEM electrolysis technology is the use of iridium, a critical raw material with high industrial demand but limited primary production, which requires – recycling. Current work presents a potentiodynamic process to dissolve Ir, as an essential step for Ir recycling. The dissolution process can be further enhanced by presence of other metal ions (*e.g.* Cu^{2+}) in the electrolyte due to cyclic deposition and stripping of the metal on Ir-oxide. The electrochemical recycling route is efficient, green and sustainable, which aligns well with SDG 7, 12, 13, & 17.

Introduction

The industry of hydrogen-based renewable power, where hydrogen is used as a power carrier, is expanding fast and is judged to have enormous potential for further growth.[1,2] Polymer electrolyte membrane (PEM) water electrolyzers (PEMWEs) and PEM fuel cells are among the prominent technologies, respectively for the electricity-to-hydrogen and the hydrogen-to-electricity conversions through electrochemical routes under acidic conditions. One of the major obstacles hindering further commercialization of these technologies is their current dependance on the platinum group metals (PGMs) and/or their compounds[1,3] as the preferred electrocatalysts to catalyze both

the cathode and anode electrochemical reactions. For example, nanosized Pt/Pt-alloys (2-5 nm) supported on carbon is used as the state-of-the-art cathode/anode electrocatalyst for PEM fuel cells, while Ir-oxide (IrO_x) is considered the most efficient and durable electrocatalyst at the PEMWE anode, where high activity towards the oxygen evolution reaction (OER), *i.e.*, the anode reaction during the electrolysis of water under acidic conditions, is essential. Apart from electrocatalysis, iridium and/or Ir-oxide nanoparticles also have versatile applications in areas including heterogeneous catalysis of chemical reactions such as hydrogenation,[4,5] in biomedicine,[6] and in sensors,[7,8] *etc.*

However, owing to the low abundance of the PGMs in the upper earth crust,[9] their large-scale extraction from the natural deposits to fulfill the growing industrial demands is neither economic nor sustainable. Therefore, recycling the PGMs from their secondary sources such as spent catalytic bodies would be inevitable to attain a continuous and sustainable supply.

[a]Department of Green Technology, University of Southern Denmark, Odense M 5230, Denmark. E-mail: rash@igt.sdu.dk; mashu@igt.sdu.dk

[b]Department for Materials Synthesis, Jozef Stefan Institute, Ljubljana 1000, Slovenia

Although the well-established pyrometallurgical and/or hydro-metallurgical routes[10–12] used for extraction of PGMs can be applied to reclaim the metals from the spent electrocatalytic bodies, there are certain disadvantages of these processes. Apart from being energy and infrastructure incentive, the conventional PGM extraction routes are unsuitable for the recovery from PEM-based electrocatalysts due to the fact that combustion of catalytic bodies typically containing perfluorinated sulfonic-acid (PFSA) ionomers produces environmentally hazardous fluorocarbons.[13,14] Therefore, an environmentally-friendly recycling of the PGM-based electrocatalysts by using mild conditions (dilute acids, no combustion)[15–19] has attracted substantial scientific and technological interests.

Electrochemical dissolution of Pt from spent PEM fuel cell electrodes is being studied by us and several other groups.[20–29] However, Ir and Ir-oxides, reputed as an extremely corrosion resistant metal, is difficult to recycle through chemical/electrochemical dissolution. However, nanoparticulate iridium-based electrocatalysts, owing to their high surface-to-volume ratio, show significant tendency towards electrochemical dissolution, especially, under the OER-active potential window, leading to a challenge for their long-term stability in the PEMWE anode electrocatalyst.[30–32] The electrochemical dissolution takes place predominantly through formation of unstable oxidation states of Ir and depends critically on the catalyst structure.[30] However, studies towards the recovery of Ir from spent PEMWEs using electrochemical dissolution are rarely reported. In a recent study, Moriau *et al.* have studied dissolution of Ir in acidic solutions (HClO$_4$ and HCl) in the presence of organic solvents and have shown an enhanced (40×) rate of Ir dissolution in the HCl-based electrolyte as compared to that in the HClO$_4$-based solution.[33] Such studies, investigating electrochemical dissolution assisted recycling of Ir-based electrocatalysts are of substantial scientific interest and technological importance.

As another aspect, to be efficient and accessible around the globe, the coming large-scale water electrolysis plants should be able to operate using low-purity waters such as seawater that contain significant amounts of metal ions among other impurities.[34] Among other challenges towards development of the impurity tolerant water electrolyzers, presence of certain impurity metal ions in the feedstock water has been reported to affect the OER activity and stability of the anode electrocatalysts adversely.[35] Therefore, further studies focused on the dissolution of Ir from the Ir-oxide anode electrocatalysts in the presence of different metal ions would benefit the development of impurity tolerant OER electrocatalysts.

We here report a study on potentiodynamic dissolution of IrO$_x$ in dilute acidic electrolytes (1 M HCl) in the presence of different metal ions. The dissolution of Ir was studied by varying different experimental parameters, namely the electrolyte compositions (type of acid, concentration of Cu^{2+} and/or presence of other metal ions) and/or the potentiodynamic treatment conditions. Different metals with standard reduction potentials ranging between ∼−0.3 V and ∼0.8 V *vs.* the reversible hydrogen electrode (RHE) were studied. Structural and electrochemical characterizations were performed to understand the effects of the metal ions on the dissolution mechanisms.

Experimental methods

Materials

Ultrapure water (Milli-Q; resistivity ≥18.2 MΩ cm at 25 °C) was used for dilution purposes to prepare the electrolytes and the catalyst dispersions. Hydrochloric acid (1 M HCl; Reagent Ph. Eur.; BDH chemicals), perchloric acid (HClO$_4$; assay: 98%, Sigma-Aldrich®), were used to prepare different aqueous electrolytes. Unless stated otherwise, high purity metal chlorides were used to prepare the electrolytes containing different metal ions. Commercially available Ir-oxide (IrO$_x$; Alfa Aesar), iso-propanol (CH$_3$–CH(OH)–CH$_3$; HPLC grade; purity: >99.9%; Sigma-Aldrich®) and perfluorinated sulfonic-acid (PFSA) ionomer dispersion (5 wt% Nafion® from Ion Power, Dupont D521) were used respectively as the model electrocatalyst, the dispersion medium along with ultrapure water, and the ionomer phase in the catalyst ink.

Working electrode preparation

The working electrode (WE) was prepared by modifying a 5 mm diameter glassy carbon (GC) rotating disc electrode (RDE) from Pine Instruments. Firstly, GC RDE was polished to mirror finish using 5 μm – followed by 0.5 μm alumina slurry. A stock solution consisting of water, isopropanol and 5 wt% Nafion® in a volumetric proportion of 78.16, 20, 1.84 was used to prepare the catalyst ink by dispersing 10 mg of the IrO$_x$ powder in 5 mL of the stock solution by ultrasonication for 60 s using a Hielscher UP200 St ultrasonic homogenizer. The ink composition was chosen to obtain a catalyst/ionomer weight ratio of 70/30. Further, the WE was prepared by drop casting 10 μL of the catalyst ink on the cleaned GC RDE and drying it at ambient conditions while spinning at 700 rpm.

Electrochemical setup and protocols

A three electrode setup consisting of the IrO$_x$ electrocatalyst modified GC RDE as the WE, a Pt counter electrode (CE) and a double junction Ag/AgCl reference electrode (RE; inner junction: sat. KCl; outer junction: sat. K$_2$SO$_4$; Aldrich) was used for the electrochemical studies. The three-electrode setup placed in a cleaned glass cell (Pyrex) containing 25 mL of an electrolyte, and it was attached to a Zahner®IM6e electrochemical workstation. The electrolyte was continuously purged with nitrogen before (*ca.* 30 min) and during the electrochemical measurements, where no rotation was applied to the WE. All the potentials measured against the Ag/AgCl RE (after ∼70% compensation of the series resistance) were converted to their corresponding values w.r.t. the RHE. In a typical experiment to study the electrochemical dissolution of Ir, the WE was subjected to a potential cycling at a specified scan rate or combination thereof between specified potential windows for specified number of cycles, as stated appropriately throughout the text. Effects of potential windows, numbers of cycles and electrolytes on the dissolution of Ir were investigated.

Dissolution quantification

The iridium amounts present on the WE (Ir-loading) were measured using an X-ray fluorescence spectrometer (XRF; Thermo Scientific Niton XL3t GOLDD + XRF analyzer). The XRF analyzer was calibrated using a procedure described in our earlier publication.[36] In brief, linear relationship between the amounts of Ir (0 µg to ∼100 µg) loading and the XRF intensity was confirmed by recording the XRF spectra for different amounts of Ir. The linear relationship was used to calibrate the instrument for determination of the Ir loadings on WE before and after the electrochemical treatment. The determined Ir-loading values were used to estimate the per cent wise degree of dissolution of Ir ($Ir_{diss}\%$) from the electrode during the electrochemical treatment (eqn (1)).

The dissolution percentage, was calculated using the following equation:

$$Ir_{diss}\% = \frac{M_0 - M_f}{M_0} \times 100 \ , \tag{1}$$

where M_0 and M_f are the initial and final loading values of Ir on the electrode, respectively.

Structural characterizations

Evolution of the structural characteristics of the IrO_x during electrochemical treatments was investigated through morphological, elemental- and surface chemical state analyses. The as-received IrO_x sample was characterized with a transmission electron microscope (TEM) using a JEOL-JEM 2100, which was operated at 200 kV. Further, bulk structural characterization through X-ray diffraction (XRD) was performed using a Rigaku Miniflex 600 X-ray diffractometer equipped with unfiltered Cu Kα radiation source. The diffractogram was recorded at a scan rate of 3° min^{-1} and at a step size of 0.02°.

Further, the IrO_x catalyst ink samples removed from the GC RDEs before and after electrochemical treatments were studied through scanning TEM (STEM) using a JEOL ARM 200CF STEM operated at 80 kV. High angle annular dark field (HAADF) and annular bright field (ABF) detectors were used simultaneously, where the collection semi angles were varied respectively between 68 and 180 mrad and between 10 and 16 mrad. The elemental compositions of the samples were determined through energy-dispersive X-ray spectroscopy (EDS) using a JEOL Centurio EDS system equipped with a 100 mm^2 silicon drift detector. Finally, surface chemical state evolution of the IrO_x samples was studied using X-ray photoelectron spectroscopy (XPS) using a SPECS® system equipped with a dual anode X-ray source and a hemispherical analyzer. Mg K$_\alpha$ (1253.6 eV) radiation was used to acquire the XPS spectra, where the pass energies for the survey and the narrow scan spectra were set respectively to 50 eV and 25 eV, with the effective spectral resolutions at 2.5 eV and 1.0 eV, respectively.

Results and discussion

Structure of IrO_x catalyst

Comprehensive structural analysis of the selected commercial IrO_x electrocatalyst has been reported in our previous study[37]
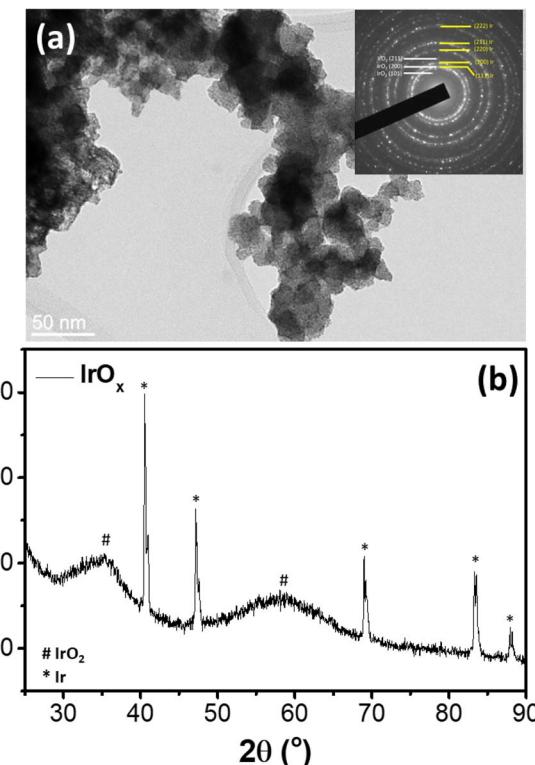

Fig. 1 (a) TEM image and (b) XRD pattern[37] of the studied IrO_x sample.

(Sample ID: IrO_x-02). In brief, as revealed from the TEM image of Fig. 1a, the IrO_x sample consists of large agglomerates (30–50 nm) of smaller nanoparticles of ∼2 nm. The inset selected area electron diffraction (SAED) pattern shows diffraction rings corresponding to metallic Ir along with low intensity rings characteristic for tetragonal (Space group $P4_2/mnm$) IrO_2.[30,38] Further the XRD pattern of the sample (Fig. 1b) also shows relatively intense and sharp diffraction peaks corresponding to metallic Ir, along with the broad diffraction peaks corresponding to tetragonal IrO_2. Hence, the sample consists of metallic Ir along with the IrO_2 nanoparticles. Our previous analysis of synchrotron XRD data confirmed the weight fractions of Ir metal and IrO_2 in the sample to be <0.1 and >0.9, respectively.[37]

Effect of metal ions on Ir dissolution

Effect of the presence of certain other metal ions on the dissolution of Ir from an IrO_x modified GC RDE subjected to a potential cycling in 1 M HCl was studied. Inspired by the enhanced dissolution of Pt found earlier through potential cycling in the presence of Cu^{2+}, different metal ions having standard reduction potentials close to that of Cu^{2+} are now studied. Here, the IrO_x modified GC RDEs (identically prepared) were subjected to an activation potential cycling (100 cycles between 0 and 1.65 V at 1 V s^{-1}) followed by a stress cycling (100 cycles between 0 and 1.65 V at 100 mV s^{-1}) in different electrolytes consisting of 1 M HCl and metal chlorides (metal ion concentration: 5 mM). A summary of the studied metal ions is shown in Table 1. It is evident that presence of Cu^{2+} enhances the Ir dissolution most efficiently, followed by Ru^{3+}, Mo^{3+}, Bi^{3+}

and Ni^{2+}. Other metal ions, namely Co^{2+}, Rh^{3+} and $[PtCl_6]^{2-}$ decrease the Ir dissolution. Owing to the highest Ir dissolution observed in its presence, this study is restricted to the Cu^{2+} ion hereafter.

To investigate the effect of anion, dissolution of Ir was also studied in 1 M HCl containing 5 mM of $CuSO_4$. As shown in Table 1, irrespective of the anion type, presence of Cu^{2+} enhances the Ir dissolution significantly. The marginally higher Ir dissolution in the presence of $CuCl_2$ compared to that in the presence of $CuSO_4$ may be attributed to factors such as (i) the measurement uncertainty, (ii) the slightly higher concentration of Cl^- in the former case and (ii) adsorption of SO_4^{2-} on the Ir-oxide surface.

Electrochemistry of IrO_x in electrolytes with/without Cu^{2+}

IrO_x electrochemistry in four different electrolytes, namely 1 M HCl, 1 M HCl + 20 mM $CuCl_2$, 0.1 M $HClO_4$ and 0.1 M $HClO_4$ + 20 mM $CuCl_2$ was studied. Fig. 2 shows the cyclic voltammograms (CVs) of the GC RDEs modified with the IrO_x electrocatalyst ink. To record the voltammogram in a certain electrolyte, the WE was activated by subjecting it to a potential cycling for 20 cycles between 0.0 and 1.2 V at a scan rate of 100 mV s^{-1}. Further, 2 cycles were recorded at a scan rate of 10 mV s^{-1} between the specified potential window and the second cycle was shown here. Although no rotation was applied to the WE for removal of the generated gas bubbles,[40] no visible accumulation of bubbles on WE was observed during the CV recording.

The CVs recorded in the absence of Cu^{2+} ions show characteristic features of the IrO_x. The broad current peak centered around 0.7 V in the negative-going scan of the CV recorded in 0.1 M $HClO_4$ (Fig. 2a) corresponds to the reduction of Ir^{4+} to Ir^{3+}, while the corresponding broad oxidation peak ($Ir^{3+} \rightarrow Ir^{4+}$) appears at ~0.8 V in the positive-going scan of the CV.[41,42] The onset of the OER can be observed in the positive-going scan at ~1.4 V. Despite the presence of metallic Ir in the sample, no activity towards hydrogen adsorption/desorption is observed for the IrO_x catalyst, unlike that reported for metallic Ir.[43,44] This

may be due to coverage of the metallic Ir core with the IrO_2 shell and hence no immediate active participation of the core in the electrochemistry. Further, the CV of the IrO_x electrocatalyst in the 0.1 M $HClO_4$ + 20 mM $CuCl_2$ electrolyte exhibits significantly different characteristics compared to that of the CV in the absence of Cu^{2+} ions. The reduction peaks corresponding to the underpotential and bulk depositions of Cu can be observed during the negative-going scan (potentials <0.4 V).[45–47] The positive-going scan shows the oxidation peaks centered at ~0.25 and ~0.55 V, corresponding to the dissolution of bulk Cu and the desorption of the underpotentially deposited Cu adlayer, respectively.[48,49] The onset of OER is not affected significantly by the presence of $CuCl_2$. However, a peak current (at 1.5 V) lower than the corresponding value in the absence of $CuCl_2$ is observed, which could be attributed to the coverage of OER active sites by adsorption of Cl^- at the potentials close to the OER onset, as reported in earlier studies on different metal surfaces such as Ir,[50] Pt,[51] Au,[52] etc.

Similarly, 1 M HCl electrolyte (Fig. 2b), the CV shows the characteristic peaks corresponding to the $Ir^{3+} \leftrightarrow Ir^{4+}$ redox couple shifted towards higher potentials by ~0.1 V compared to the corresponding peaks in 0.1 M $HClO_4$. The current value at 1.5 V is observed to be higher compared to that in 0.1 M $HClO_4$ electrolyte, and a reduction peak at ~1.25 V during the negative-going scan is observed. The observations may respectively be attributed to the evolution of Cl_2 and the reduction of the surface adsorbed Cl ($Cl + e^- \rightarrow Cl^-$). In the presence of Cu (electrolyte: 1 M HCl + 20 mM $CuCl_2$), deposition of Cu for the potentials <0.5 V during negative-going cycle is evident. However, the extent of Cu deposition is reduced significantly compared to that in the 0.1 M $HClO_4$ + 20 mM $CuCl_2$ electrolyte. Similarly, the Cu stripping peaks (bulk/underpotentially deposited Cu) are not prominent. Also, the Cl-reduction peak at ~1.25 V during the negative-going scan shows relatively reduced intensity compared to that in 1 M HCl, probably due to the surface deposition of more stable species such as Cu-oxides on the IrO_x electrocatalyst that limit access to the active sites for Cl^- adsorption.

Table 1 Standard reduction potentials and Ir dissolution% for different electrolytes with/without metal ions (concentration: 5 mM, respectively) in 1 M HCl

Metal ion (M^{x+})/complex	Counter ion	Standard reduction potential (V)[39] ($M^{x+} \rightarrow M^0$)	Ir dissolution (%)
Rh^{3+}	Cl^-	0.758	13
Co^{2+}	Cl^-	−0.280	13
Ni^{2+}	Cl^-	−0.257	20
Mo^{3+}	Cl^-	−0.200	23
Bi^{3+}	Cl^-	0.308	21
Cu^{2+}	Cl^-	0.342	34
Cu^{2+}	SO_4^{2-}	0.342	32
Ru^{3+}	Cl^-	0.249 ($Ru^{3+} \rightarrow Ru^{2+}$)	32
		0.455 ($Ru^{2+} \rightarrow Ru$)	
Rh^{3+}	Cl^-	0.758	13
$[PtCl_6]^{2-}$	H^+	0.775 ($[PtCl_6]^{2-} + 2e^- \rightarrow [PtCl_4]^{2-} + 2Cl^-$)	7
		0.68 ($[PtCl_4]^{2-} + 2e^- \rightarrow Pt + 4Cl^-$)	
None	NA	0.866 ($[IrCl_6]^{3-} + 3e^- \rightarrow Ir + 6Cl^-$)	16
		0.77 ($Ir^{3+} \rightarrow Ir$)	
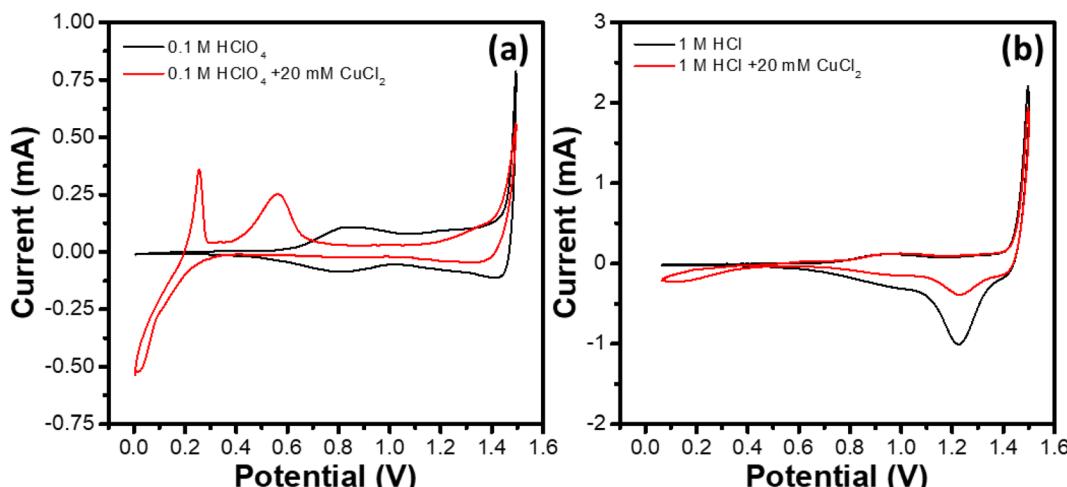
Fig. 2 Cyclic voltammograms of WE (IrO$_x$ modified GC RDE) recorded at a scan rate of 10 mV s^{-1} in (a) 0.1 M HClO$_4$ and 0.1 M HClO$_4$ + 20 mM CuCl$_2$, and (b) 1 M HCl and 1 M HCl + 20 mM CuCl$_2$ electrolytes saturated with nitrogen (room temperature, no rotation of WE).

Potentiostatic dissolution of Ir

For a fair comparison, Ir dissolution in the 1 M HCl and 1 M HCl + 20 mM CuCl$_2$ electrolytes in the absence of an applied potential was studied by holding the identically prepared IrO$_x$ modified GC RDEs in the electrolytes for 60 min, a time equivalent to those required in the experiments involving electrochemical treatments (activation and potential cycling). Furthermore, the effect of convection in the electrolyte on the Ir dissolution was also studied by holding the same electrode for another 60 min while stirring the electrolyte. As shown in Table 2, no significant dissolution of Ir from the IrO$_x$ modified GC RDE takes place in either of the electrolyte (with/without Cu^{2+}). Also, stirring the electrolytes at 500 rpm did not enhance the Ir loss from the electrode, which confirmed the IrO$_x$ coating on the GC RDE to be robust and excluded the possibility of significant Ir loss due to physical detachment of the catalyst layer during the potentiodynamic treatments. It is also noticeable that the Ir losses (wt%) for initial holding for 60 min. in still electrolytes are higher compared to those observed for the holding the same electrodes in the electrolytes being stirred. However, the Ir losses due to holding with/without stirring are insignificant compared to those observed during the experiments involving potentiodynamic treatments. Again, as Cu^{2+} can reduce to Cu$^+$ in chloride baths[53,54] and the later may be responsible for the enhanced Ir dissolution in the presence of Cu^{2+}, effect of the presence of Cu$^+$ on Ir dissolution

was studied by exposing the Ir-oxide coated electrode to the 1 M HCl + 20 mM CuCl electrolyte for 60 min (no potential applied). As shown in Table 2, no significant dissolution of Ir takes place in the presence of Cu$^+$. This confirms that the Ir dissolution mechanism may not be attributed to the formation of Cu$^+$ intermediate and its reaction with the Ir-oxide.

Potentiodynamic dissolution of Ir below OER onset potentials (0.1 to 1.2 V)

This set of experiments consisted of four identically prepared WEs subjected to a potentiodynamic treatment in different electrolytes, namely 1 M HClO$_4$, 1 M HClO$_4$ + 20 mM CuCl$_2$, 1 M HCl and 1 M HCl + 20 mM CuCl$_2$. The potentiodynamic treatment consisted of (i) activation cycling for 20 cycles at 100 mV s^{-1} between 1.2 and 0.0 V (start potential: 1.2 V, end potential: 1.2 V), (ii) stress cycling for 1600 cycles at 1 V s^{-1} between 1.2 and 0.1 V (start potential: 1.2 V, end potential: 1.2 V) along with (iii) intermittent observation cycling for 2 cycles at 10 mV s^{-1} between 1.2 and 0.1 V (start potential: 1.2 V, end potential: 1.2 V) after specified number (0, 20, 100, 200, 300, 400, 500, 600, 800, 1000, 1200, 1400 and 1600) of stress cycles. The second cycle of the observational CV recorded after the 0th and the 1600th stress cycles, labeled respectively as the initial and final CVs, are shown in Fig. 3a–d for different electrolytes studied here.

As can be seen in Fig. 3a, no significant difference in the initial and final CV plots has been observed in 1 M HClO$_4$

Table 2 Ir dissolution from the IrO$_x$ modified GC RDE without applied potentials with/without electrolyte stirring

Electrolyte composition	Treatment	Ir dissolution (%)
1 M HCl	Holding for 60 min without stirring; no potential applied	1.7
1 M HCl	Holding for 60 min with stirring (rpm 500); no potential applied	1.1
1 M HCl + 20 mM CuCl$_2$	Holding for 60 min without stirring; no potential applied	1.8
1 M HCl + 20 mM CuCl$_2$	Holding for 60 min with stirring (rpm 500); no potential applied	0.2
1 M HCl + 20 mM CuCl	Holding for 60 min without stirring; no potential applied	0.3

electrolyte. The CVs show the current peaks corresponding to the $Ir^{3+} \leftrightarrow Ir^{4+}$ redox couple, as described earlier. Weak peaks corresponding to hydrogen adsorption (negative-going scan; potential <0.4 V) and desorption (positive-going scan; potential <0.4 V) are also observed for the initial CV, which become less significant for the final CV after 1600 stress cycling. Initial and final CVs for the WE subjected to the stress cycling in 1 M HCl (Fig. 3b) show similar characteristics in the hydrogen adsorption/desorption region. However, compared to that in 1 M HClO$_4$ electrolyte, the $Ir^{3+} \leftrightarrow Ir^{4+}$ redox couple for the initial CV in 1 M HCl shifts towards higher potentials. For the final CV, the shift increases further towards higher potentials, especially for the oxidation reaction ($Ir^{3+} \rightarrow Ir^{4+}$) during positive-going scan.

Initial and final CVs for the 1 M HClO$_4$ + 20 mM CuCl$_2$ and the 1 M HCl + 20 mM CuCl$_2$ electrolytes are shown respectively in Fig. 3c and d, where the CVs exhibit characteristic features corresponding to Cu deposition and dissolution and the $Ir^{3+} \leftrightarrow Ir^{4+}$ redox couple. Notably, in both the electrolytes containing Cu^{2+}, the region corresponding to the $Ir^{3+} \leftrightarrow Ir^{4+}$ redox couple shrinks during the stress cycling. Table 3 summarizes the per cent wise dissolution of Ir during the stress cycling in different

electrolytes. It is evident that presence of Cu^{2+} enhances the Ir dissolution significantly by factors of 7.7 and 9.4 for 1 M HClO$_4$ and 1 M HCl electrolytes, respectively. As a higher per cent wise dissolution of Ir takes place in the HCl based electrolytes as compared to that in the HClO$_4$ based electrolytes, hereafter, this study focuses on the former.

Ir dissolution through potential cycling across the OER onset potential

In this set of experiments, IrO$_x$ modified GC RDEs were subjected to potential cycling between 0.0 and 1.65 V (both the start and the end potentials being 1.2 V) in 1 M HCl containing different concentrations of CuCl$_2$. CV plots shown in Fig. 4a and b correspond to potential cycling of the IrO$_x$ modified GC RDEs for 200 cycles at 100 mV s^{-1}, respectively in 1 M HCl and 1 M HCl + 5 mM CuCl$_2$ electrolytes.

Initial (1st stress cycle) and final (200th stress cycle) highlighted with thick lines show significant evolution of the CVs during the potential cycling. The peaks corresponding to the $Ir^{3+} \leftrightarrow Ir^{4+}$ redox couple shrink significantly. Also, the current values at 1.65 V, which correspond to the OER and the chlorine
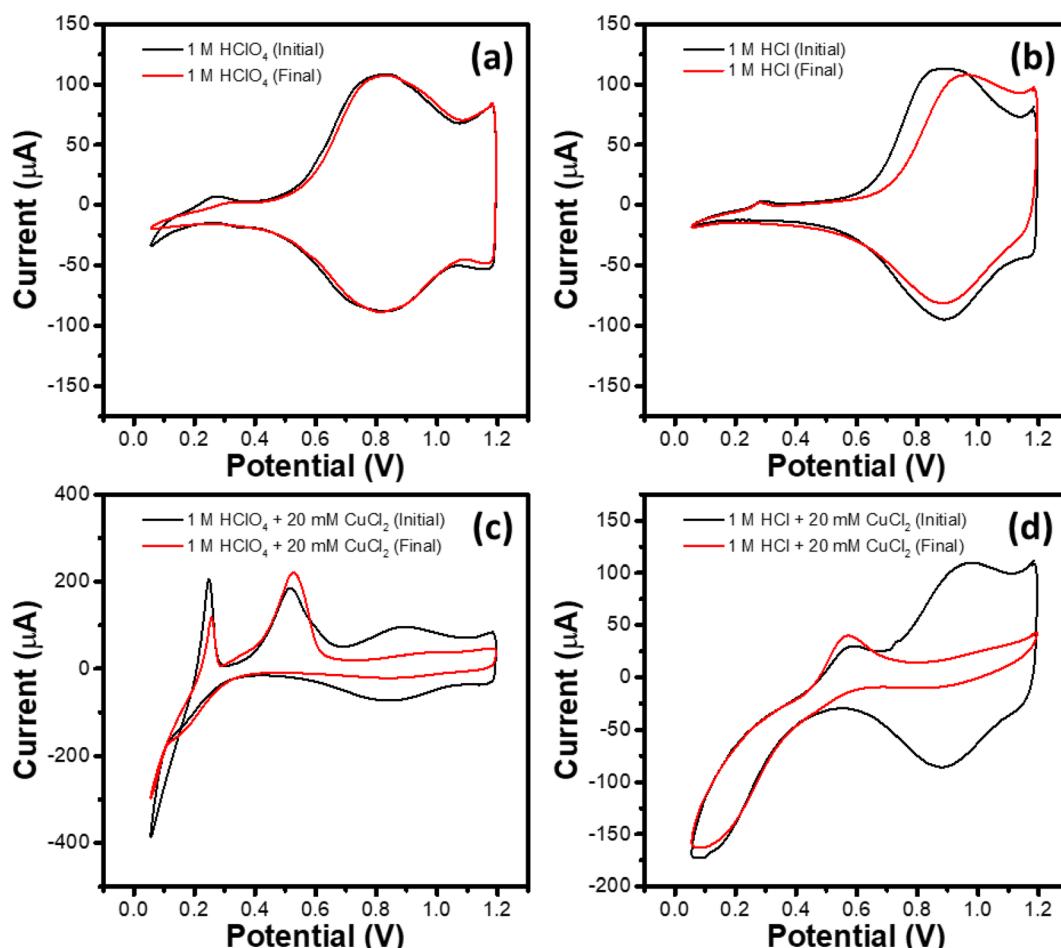
Fig. 3 CV plots of the IrO$_x$ modified GC RDEs recorded at a scan rate of 10 mV s^{-1} in nitrogen saturated (a) 1 M HClO$_4$, (b) 1 M HCl (c) 1 M HClO$_4$ + 20 mM CuCl$_2$, and (d) 1 M HCl + 20 mM CuCl$_2$ electrolytes. Labels initial and final correspond respectively to the electrodes subjected to 0 and 1600 stress cycles between 0.1 and 1.2 V at a scan rate of 1.0 V s^{-1}.

Table 3 Effect of presence of Cu^{2+} on the dissolution of Ir from the IrO_x modified GC RDE during the stress cycling below OER onset in different electrolytes

Electrolyte	Ir loading (μg)		Ir dissolution (%)	Dissolution enhancement factor
	Initial	Final		
1 M $HClO_4$	15.9	15.6	1.5	1.0
1 M HCl	17.6	17.2	2.2	1.0
1 M $HClO_4$ + 20 mM $CuCl_2$	16.8	14.9	11.3	7.7
1 M HCl + 20 mM $CuCl_2$	16.8	13.4	20.5	9.4

evolution reaction collectively, by ∼67% and ∼71% for the 1 M HCl and 1 M HCl + 5 mM $CuCl_2$ electrolytes, respectively (Fig. 4c). Hence, presence of Cu^{2+} does not affect the oxygen and chlorine evolutions significantly. On the other hand, as depicted in Fig. 4d, the % dissolution of Ir from the electrodes during the potential cycling is affected significantly by the presence of Cu^{2+}, showing the values of ∼16% and ∼40% for the 1 M HCl and 1 M HCl + 5 mM $CuCl_2$ electrolytes, respectively. This clearly confirms enhancement of Ir dissolution in the presence of Cu^{2+}.

Moreover, the Ir dissolution in 1 M HCl (with/without Cu^{2+}) increases significantly compared to that observed for the potential cycling below OER onset potentials.

Effect of Cu^{2+} concentration, number of potential cycles and/ or scan rate

Variation of the Ir dissolution from the IrO_x modified GC RDEs during potential cycling with the concentration of Cu^{2+} in 1 M
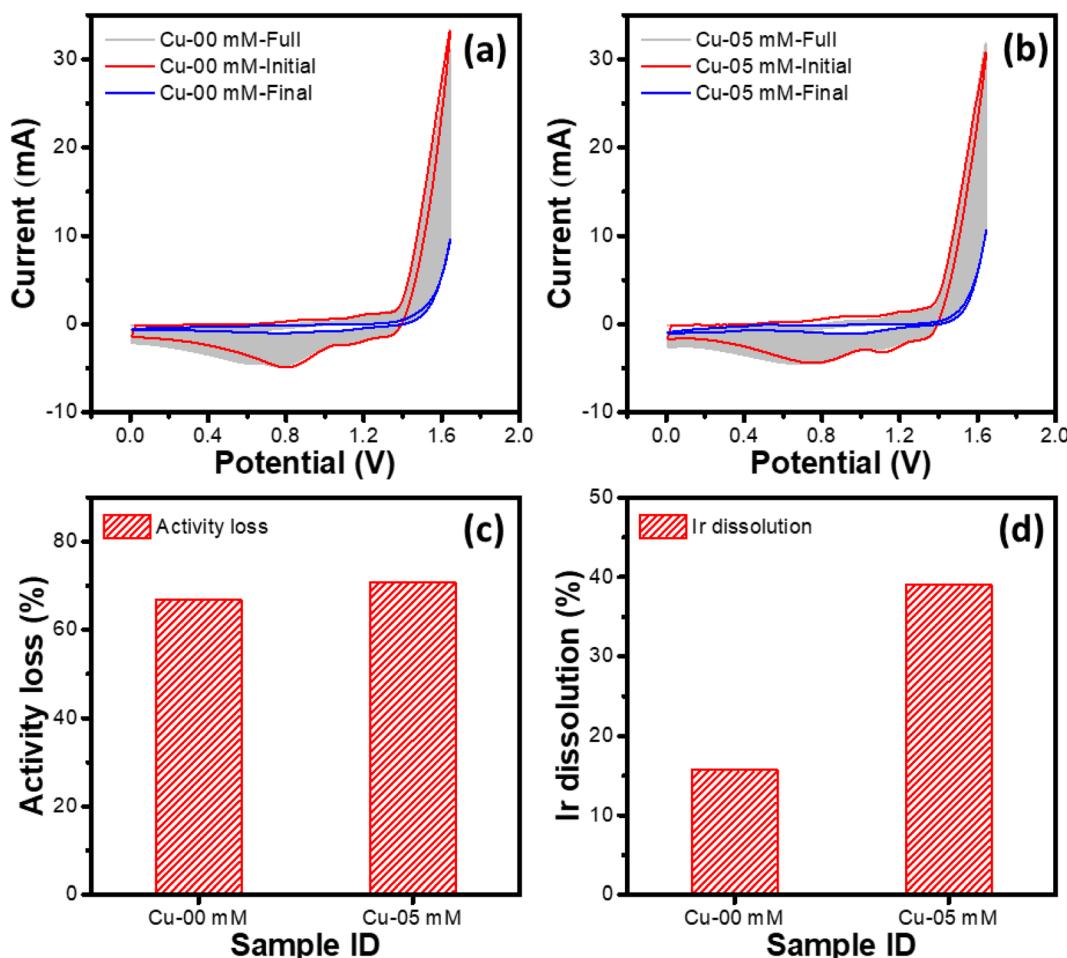

Fig. 4 (a and b) CV plots corresponding to potential cycling of the IrO_x modified GC RDEs for 200 cycles at 100 mV s^{-1} in (a) 1 M HCl and (b) 1 M HCl + 5 mM $CuCl_2$ electrolytes. Initial (1st stress cycle) and final (200th stress cycle) have been highlighted with thick lines, while other cycles appear as a gray continuum. Variations of (c) the loss of oxygen and chlorine evolution activities (combined) in terms of percentage change in the current at 1.65 V and (d) the dissolution of Ir (%) from the GC RDEs during the potential cycling in different electrolytes, namely 1 M HCl (Cu-00 mM) and 1 M HCl + 5 mM $CuCl_2$ (Cu-05 mM).

HCl was studied. In this set of experiments, identically prepared WEs (IrO$_x$ modified GC RDEs) were subjected to an electrochemical treatment consisting of activation cycling (100 cycles between 0 and 1.65 V at 1.0 V s; start potential: 1.2 V, end potential: 1.2 V) followed by stress cycling for another 100 cycles between 0 and 1.65 V at 100 mV s^{-1} (start potential: 1.2 V, end potential: 1.2 V) in different electrolytes, consisting of 1 M HCl and varying concentrations (0, 5, 20 and 50 mM) of CuCl$_2$.

As depicted in Fig. 5a, it is evident that the dissolution of Ir increases with increasing the concentration of Cu^{2+}, however, with a decreasing differential change, suggesting saturation of the Ir dissolution rate for high concentrations of Cu^{2+} (1st derivative of the Ir dissolution $vs.$ Cu^{2+} concentration curve; Fig. 5a). Similar relationship is also observed between the number of stress cycles and the Ir dissolution rate (Fig. 5b), where the differential change in the dissolution decreases with increasing number of potential cycling. The activation treatment at a faster scan rate (1 V s^{-1}) for 100 cycles leads to relatively smaller Ir dissolution compared to that for the potential cycling at a slower scan rate (100 mV s^{-1}).

Structural characterizations and mechanism discussion

Structural characterizations on the untreated and the electrochemically treated IrO$_x$ samples collected from the GC RDEs were performed to gain the mechanistic insights into the dissolution of Ir during electrochemical treatment. Untreated and electrochemically treated samples collected from the GC RDE were analyzed for their morphological, elemental – and surface chemical characteristics, respectively through high resolution TEM, EDS and XPS techniques. The electrochemically treated samples were prepared by potential cycling of the IrO$_x$ modified GC RDEs between 0.0 and 1.65 V for 100 cycles at 1 V s^{-1} and another 100 cycles at 100 mV s^{-1} in two different electrolytes, namely 1 M HCl and 1 M HCl + 20 mM CuCl$_2$. To be comparable, the untreated sample was also prepared by modifying a GC RDE by drop-casting 10 µL of the IrO$_x$ catalyst ink and drying at 700 rpm under ambient conditions.

Surface morphology and elemental analysis

High-resolution HAADF-STEM images of the untreated and the electrochemically treated samples are shown in Fig. 6. The untreated IrO$_x$ sample consists of agglomerated globular particles (∼20 nm) densely covered with small nanoparticles of < 2 nm in size (Fig. 6a and b). Micrographs of the samples subjected to the stated stress cycling in 1 M HCl electrolyte (Ir dissolution: ∼16%) shown in Fig. 6c and d exhibit a microstructure like that of the untreated sample. Again, the microstructure does not change appreciably for the IrO$_x$ sample stress cycled in 1 M HCl + 20 mM CuCl$_2$ electrolyte (Ir dissolution: ∼45%), as can be seen from the corresponding images of Fig. 6e and f.

Furthermore, EDS mapping of different samples show similar elemental distributions with no evidence of presence of Cu in the sample exposed to the Cu^{2+} containing electrolyte (Fig. 7 and 8). This could be attributed to the fact that as the end potential for the electrochemical dissolution experiments was set to 1.2 V, no Cu is expected to be deposited on the electrode at that potential. Further, small amounts of Cu being adsorbed on the Ir-oxide on the electrode might be expected. However, as the Cu Kα peak is overlapping with a very small Ir L1 peak, while a smaller Cu Kβ peak is close to an onset of intensive Ir Lα peak, which makes it extremely difficult to observe small amounts of Cu in the sample.

The EDS analysis showing the similar elemental distributions for different samples and the microstructural analysis of the samples do not indicate preferred dissolution of certain morphological features of the samples. The observation could indicate the observed Ir dissolution taking place through complete dissolution of the exposed Ir nanoparticles and hence unveiling the inner nanoparticles from the agglomerates, which were obscured by those removed through dissolution.

Surface chemical state

XPS survey spectra of the untreated and electrochemically treated samples are shown in Fig. 9a. All the three samples show
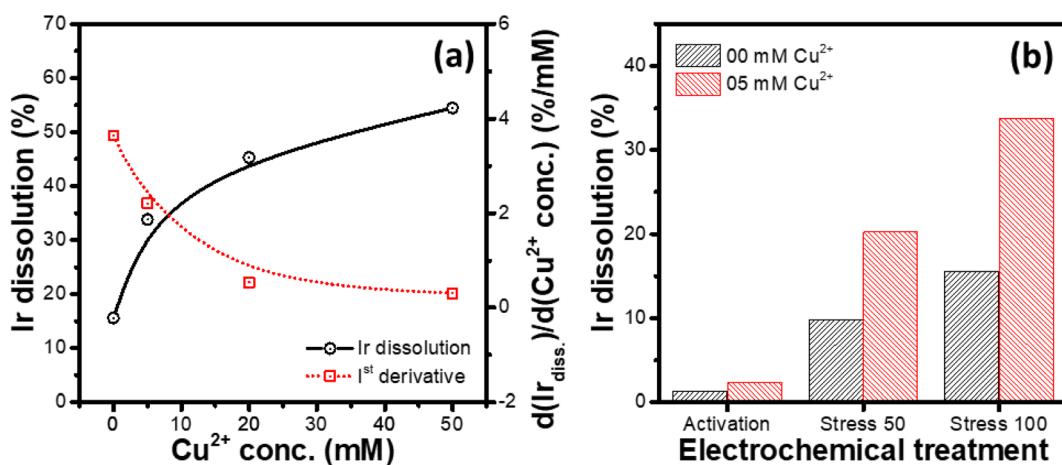

Fig. 5 (a) Variations of the Ir dissolution its first derivative with the Cu^{2+} concentration. (b) Effect of different electrochemical treatments on the Ir dissolution (activation: 100 cycles, 1 V s^{-1}, 0–1.65 V; stress 50: activation + 50 stress cycles, 100 mV s^{-1}, 0–1.65 V; stress 100: activation + 100 stress cycles, 100 mV s^{-1}, 0–1.65 V) in 1 M HCl and 1 M HCl + 5 mM CuCl$_2$ electrolytes, respectively.
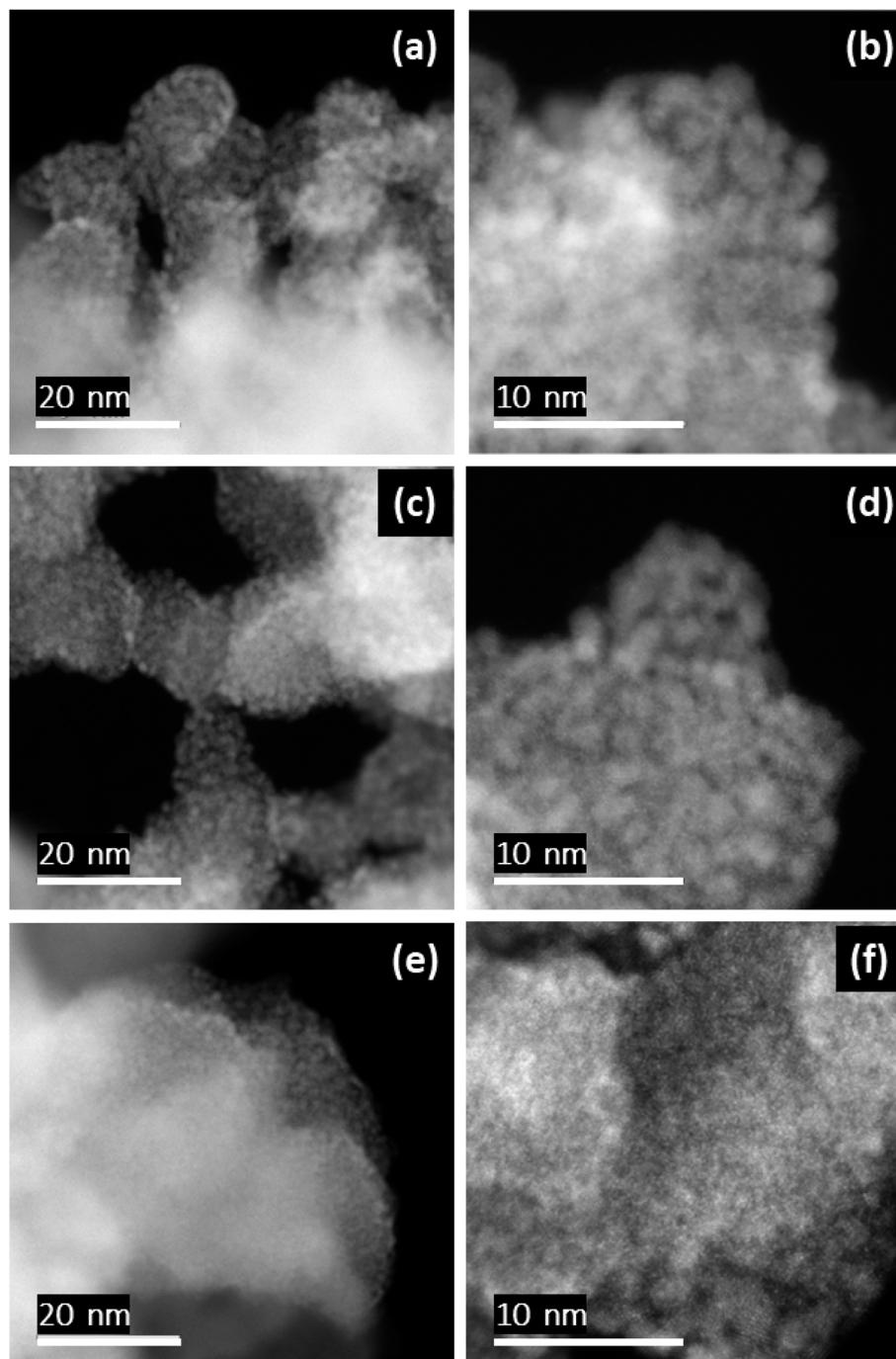
Fig. 6 HAADF STEM images of (a and b) the untreated IrO$_x$ sample, and the electrochemically treated (100 cycles, 0.0–1.65 V, 100 mV s^{-1}) IrO$_x$ samples in (c and d) 1 M HCl and in (e and f) 1 M HCl + 20 mM CuCl$_2$ electrolytes.

presence of Ir, O, C and F. However, no peak corresponding to Cu was observed for the sample exposed to the Cu^{2+} containing electrolyte, which agrees with the observation made from the EDS analysis. The surface elemental composition of the studied samples is shown in the inset table of Fig. 9a. Here, presence of F 1s peak is due to the Nafion® ionomer in the catalyst ink, while the C 1s peak has contributions from the sample support and the adventitious carbon, apart from the carbon in the ionomer. Due to this complex contributions in the C 1s signal,

the adventitious carbon peak at ∼284.7 eV [55] could not be used for the binding energy (BE) calibration. Again, the O 1s peak originates from the oxygen functional groups on support/ adventitious carbon, the IrO$_x$ and the ionomer phase. Hence, the variations of the relative abundances of C, O and F is not relevant for the Ir dissolution interpretation. The lower abundance of Ir in the untreated sample may be attributed to the coverage of the IrO$_x$ nanoparticles with the ionomer, leading to lower Ir signal. The electrochemical treatment leads to ionomer
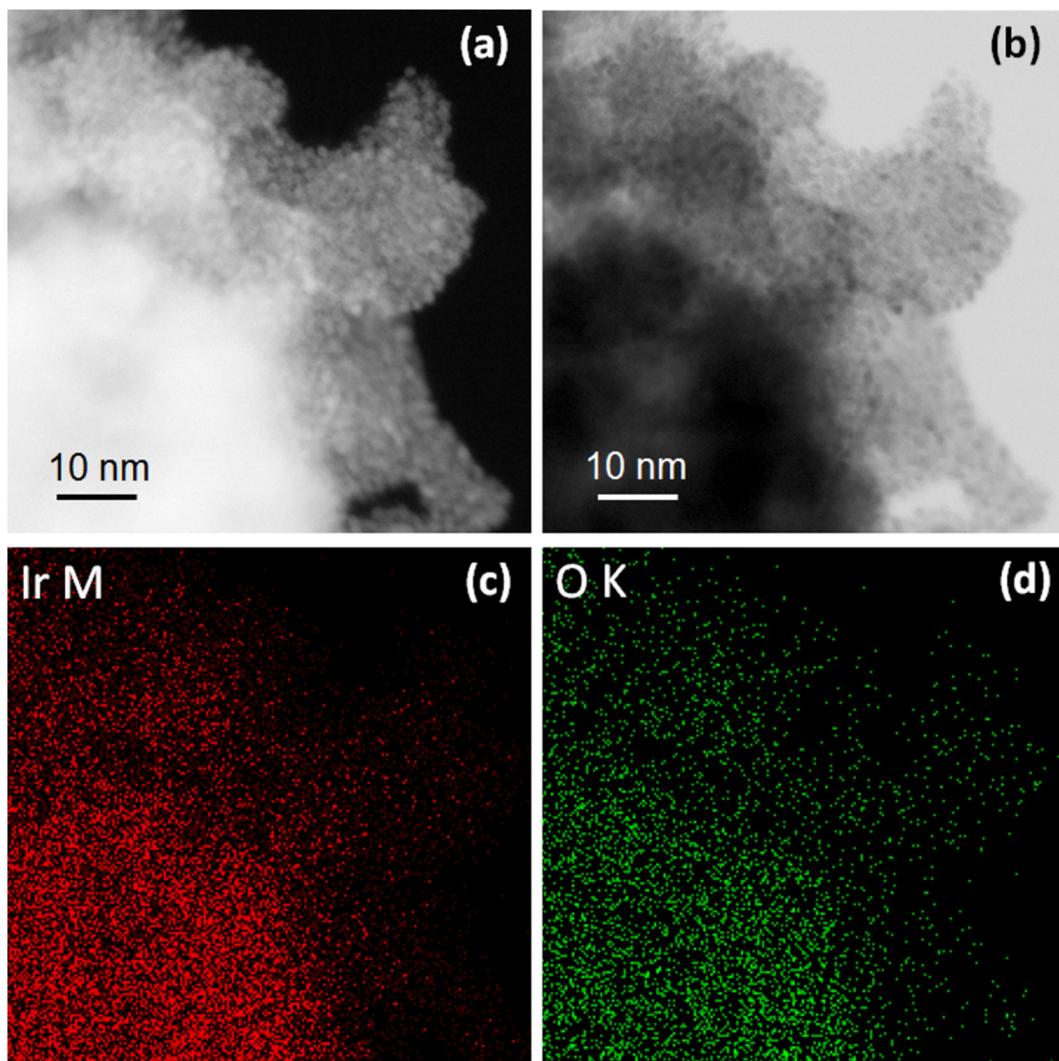
Fig. 7 HAADF (a) and BF (b) STEM images and corresponding elemental maps for Ir (c) Ir and O (d) for IrO_x sample treated electrochemically in 1 M HCl.

degradation, exposing the IrO_x surface and hence increasing the relative Ir signal despite lower Ir content in the sample.

The high-resolution C 1s spectra of the studied samples shown in Fig. 9b show peaks corresponding to C–C/C=O (BE range: 285–287 eV) and $CF/CF_2/CF_3$ (BE range: 291–295 eV) bonds.[56–60] The C 1s spectra of the electrochemically treated samples are significantly different compared to that for the untreated sample. The difference could be attributed to the degradation of the ionomer during potential cycling, as discussed in previous reports.[57,59–63] Similarly, the high-resolution O 1s spectra shown in Fig. 9c correspond to different bonds such as C–O, Ir–O, O–H *etc.*,[58,64] which show significant impact of the potential cycling in terms of the envelope shift towards lower BE values. However, as detailed analysis of the ionomer degradation is not intended in this study, so a deconvolution and detailed analysis of the C 1s and O 1s spectra is not considered here.

High resolution Ir 4f spectra of the studied samples exhibit the $4f_{5/2}$ and $4f_{7/2}$ peak components separated by ∼3 eV.[65] The samples show similar Ir 4f spectra, as indicated by the $4f_{5/2}$ component positions in the spectra (dashed vertical line in Fig. 9d), which appear at the BE value of 63.5 eV for all the studied samples. Hence, the untreated and electrochemically treated samples show similar surface chemistry of Ir, which agrees with the observations made from the microstructural analysis, *i.e.*, part of the IrO_x, which is exposed to the electrolyte, gets dissolved, leaving the undissolved sample unaffected structurally and chemically.

Discussion on dissolution enhancement mechanism in the presence of metal ions

As reported previously for Pt-based electrocatalysts, enhancement of the dissolution of Pt in the presence of Cu^{2+} has been attributed to the inhibition of the Ostwald ripening through redeposition of the dissolved Pt species on the undissolved Pt nanoparticles.[22] The underpotential deposition of Cu on the Pt surface reduces the probability of redeposition of the Pt species, which leads to enhancement of the Pt dissolution. However,
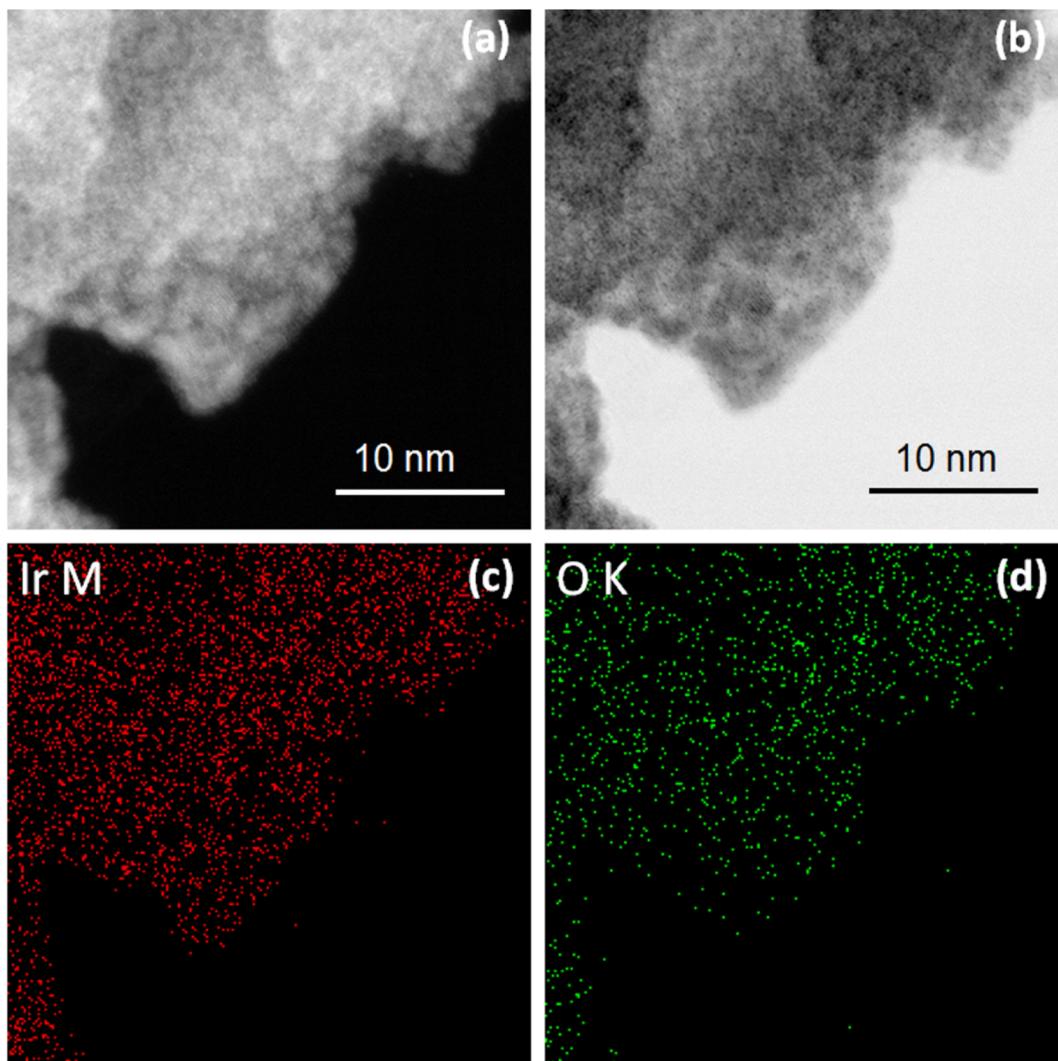
Fig. 8 HAADF (a) and BF (b) STEM images and corresponding elemental maps for Ir (c) Ir and O (d) for IrO_x sample treated electrochemically in 1 M HCl + 20 mM $CuCl_2$.

microstructural analysis of the IrO_x samples subjected to the potentiodynamic treatments shows no sign of Ostwald ripening for the IrO_x dissolution experiments in different electrolytes with/without Cu. Therefore, the enhancement of Ir dissolution is not related to the Ostwald ripening inhibition observed in case of Pt. Furthermore, the XPS analysis of the undissolved IrO_x samples (after potentiodynamic treatment) suggests that the surface chemical state of Ir is unaltered. This could be attributed to the dissolution of Ir in the oxide surface layers that speeds up through cyclic deposition and stripping of the Cu layer, as evidenced by the presence of corresponding peaks in the cyclic voltammograms recorded in the Cu^{2+} containing electrolytes (Fig. 3c–d). The stripping of Cu during the positive-going scan probably removes the top IrO_x layer through weakening the Ir–O–Ir bonds. The effect thus depends on the nature of the interaction between the Ir and O and M bonds, leading to significantly different effects of different metal ions, $e.g.$, decreased dissolution in the presence of Rh^{3+} and enhanced dissolution when Cu^{2+}, Bi^{3+} or Ru^{3+} ions attach to the oxide surface.

The proposed mechanism is also supported by the observation that the presence of Cu^+ was not found to be involved in the dissolution mechanism. Finally, as shown in Table 4, holding at a constant potential (reducing or oxidizing) does not lead to an enhanced dissolution in the presence of Cu^{2+} compared to that in the absence of it, though it is clear that oxidizing condition leads to higher degree of Ir dissolution. Thus, the potential cycling is observed to be the essential part of the enhancement of Ir dissolution.

Applicability perspective

The observed enhancement of the dissolution of Ir through potential cycling of the electrodes consisting of the Ir-oxide electrocatalyst may be developed as an electrochemical route for recovering Ir from the acidic electrolyzer MEAs containing fluoropolymers that produce hazardous emissions when subjected to conventional pyrometallurgical procedures. While the presence of metal ions such as Cu^{2+} enhances the dissolution rate significantly, recovery of Ir from the dissolution bath
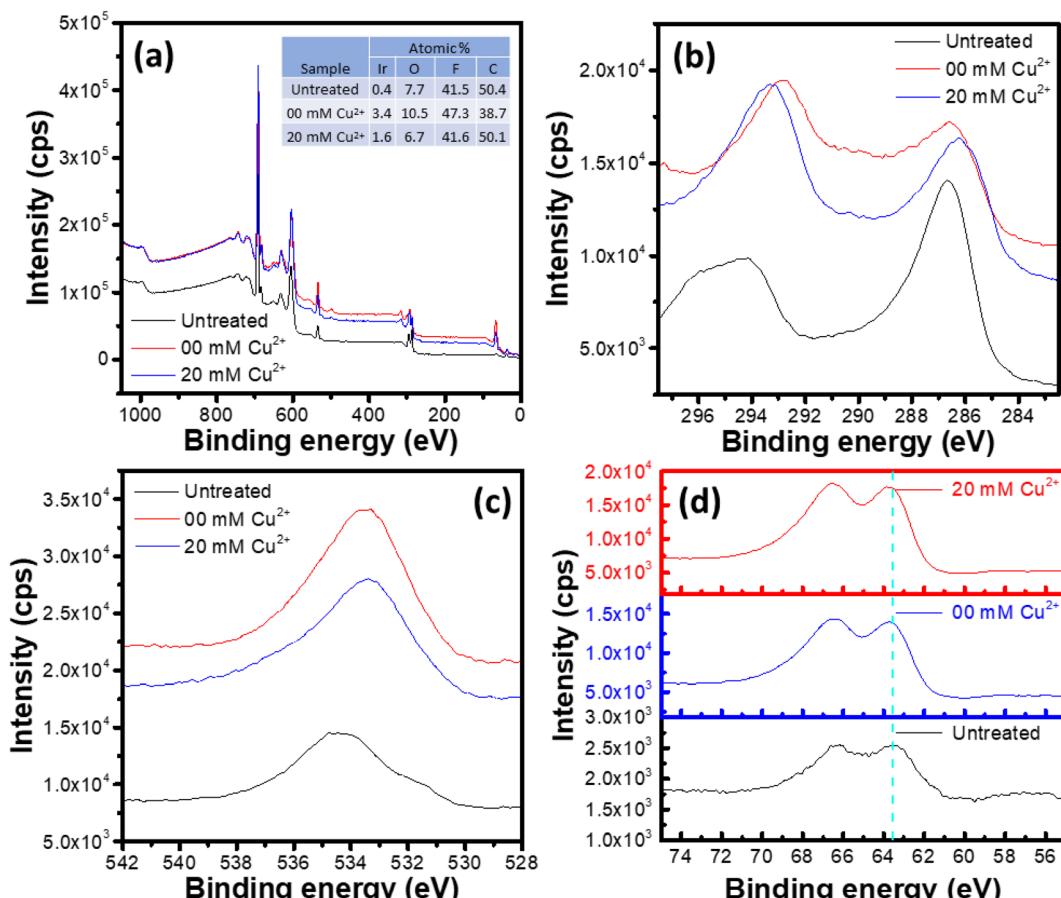
Fig. 9 (a) XPS survey spectra of the untreated IrO_x and the electrochemically treated IrO_x samples prepared by potential cycling between 0.0 and 1.65 V for 100 cycles at 1 V s^{-1} and another 100 cycles at 100 mV s^{-1} respectively in two electrolytes, namely 1 M HCl (00 mM Cu^{2+}) and 1 M HCl + 20 mM $CuCl_2$ (20 mM Cu^{2+}). Inset table shows the surface elemental composition of the samples. Narrow scan XPS spectra corresponding to (b) C 1s, (c) O 1s and (d) Ir 4f peaks.

Table 4 Chronoamperometric dissolution of Ir in different dissolution baths and at different potentials

Electrolyte	Applied potential (V)	Holding time (min)	Ir dissolution (%)
1 M HCl	0.0	60	1.5
1 M HCl + 5 mM $CuCl_2$	0.0	60	3.4
1 M HCl	1.5	60	11.0
1 M HCl + 5 mM $CuCl_2$	1.5	60	10.2

containing both the dissolved Ir species and the additive metal ions may be achieved by conventional hydrometallurgical routes. For example, oxidation of the Ir^{3+} to Ir^{4+} followed by selective precipitation.[66–68] However, in present work, such recovery of Ir was out of the scope of the current study.

Conclusions

In conclusion, the electrochemical dissolution of IrO_x in the presence of different metal ions has been studied. Presence of Cu^{2+f} in the HCl-based electrolyte shows the highest percent

wise dissolution of Ir during potential cycling. Compared to that in 1 M HCl, the Ir dissolution enhances by a factor of ~3 during potential cycling between 0.0 and 1.65 V. Enhancement of the dissolution of Ir is also observed in the presence of other metal ions such as Ni^{2+}, Mo^{3+}, Bi^{3+}, Ru^{3+}, *etc.*, while presence of an ion/complex such Co^{2+}, Rh^{3+} and $[PtCl_6]^{2-}$ lowers the Ir dissolution. This study could provide important ideas for development of impurity tolerant acidic water electrolyzers, where dissolution of the electrocatalyst must be minimized. On the other hand, enhancement of the Ir dissolution through potential cycling in the presence of metal ions such as Cu^{2+} provides an encouraging route for recovery of Ir from the Ir-based spent OER electrocatalysts through electrochemical dissolution.

Conflicts of interest

There are no conflicts to declare.

Acknowledgements

References

1 Y. Wang, Y. Pang, H. Xu, A. Martinez and K. S. Chen, *Energy Environ. Sci.*, 2022, **15**, 2288–2328.

2 S. A. Grigoriev, V. N. Fateev, D. G. Bessarabov and P. Millet, *Int. J. Hydrogen Energy*, 2020, **45**, 26036–26058.

3 S. Shiva Kumar and V. Himabindu, *Mater. Sci. Energy Technol.*, 2019, **2**, 442–454.

4 H.-y. Jiang, J. Xu and B. Sun, *Appl. Organomet. Chem.*, 2018, **32**, e4260.

5 D. Xu, P. Diao, T. Jin, Q. Wu, X. Liu, X. Guo, H. Gong, F. Li, M. Xiang and Y. Ronghai, *ACS Appl. Mater. Interfaces*, 2015, **7**, 16738–16749.

6 S. M. King, S. Claire, R. I. Teixeira, A. N. Dosumu, A. J. Carrod, H. Dehghani, M. J. Hannon, A. D. Ward, R. Bicknell, S. W. Botchway, N. J. Hodges and Z. Pikramenou, *J. Am. Chem. Soc.*, 2018, **140**, 10242–10249.

7 M. Cui, J. Zhou, Y. Zhao and Q. Song, *Sens. Actuators, B*, 2017, **243**, 203–210.

8 M. Zea, A. Moya, M. Fritsch, E. Ramon, R. Villa and G. Gabriel, *ACS Appl. Mater. Interfaces*, 2019, **11**, 15160–15169.

9 R. L. Rudnick and S. Gao, in *Treatise on Geochemistry*, ed. H. D. Holland and K. K. Turekian, Pergamon, Oxford, 2003, pp. 1–64, DOI: 10.1016/B0-08-043751-6/03016-4.

10 C. Saguru, S. Ndlovu and D. Moropeng, *Hydrometallurgy*, 2018, **182**, 44–56.

11 Z. Peng, Z. Li, X. Lin, H. Tang, L. Ye, Y. Ma, M. Rao, Y. Zhang, G. Li and T. Jiang, *JOM*, 2017, **69**, 1553–1562.

12 C. Liu, S. C. Sun, X. P. Zhu, G. F. Tu and J. Y. Zhang, *IOP Conf. Ser.: Mater. Sci. Eng.*, 2019, **479**, 012058.

13 T. Stoiber, S. Evans and O. V. Naidenko, *Chemosphere*, 2020, **260**, 127659.

14 M. Feng, R. Qu, Z. Wei, L. Wang, P. Sun and Z. Wang, *Sci. Rep.*, 2015, **5**, 9859.

15 B. J. Smith, D. J. Graziano, M. E. Riddle, D.-J. Liu, P. Sun, C. Iloeje, E. Kao and D. Diamond, *Platinum Group Metal Catalysts-Supply Chain Deep Dive Assessment, USDOE Office of Policy (PO)*, 2022.

16 N. Hodnik, C. Baldizzone, G. Polymeros, S. Geiger, J.-P. Grote, S. Cherevko, A. Mingers, A. Zeradjanin and K. J. Mayrhofer, *Nat. Commun.*, 2016, **7**, 13164.

17 R. Sharma, M. J. Larsen, L. C. Larsen, A. Bogø, L. Grahl-Madsen and S. M. Andersen, *Sustainable Energy Fuels*, 2022, **6**, 5177–5186.

18 L. Duclos, R. Chattot, L. Dubau, P.-X. Thivel, G. Mandil, V. Laforest, M. Bolloli, R. Vincent and L. Svecova, *Green Chem.*, 2020, **22**, 1919–1933.

19 J. Cui, F. Yu, M. Tian, C. Yan, T. Shen, X. Wang, U. H. Prova, C. Wang, G. Huang and S. Xu, *Green Chem.*, 2023, **25**, 9209–9217.

20 R. Sharma, K. R. Nielsen, P. B. Lund, S. B. Simonsen, L. Grahl-Madsen and S. M. Andersen, *ChemElectroChem*, 2019, **6**, 4471–4482.

21 R. Sharma, S. Gyergyek and S. M. Andersen, *ChemSusChem*, 2018, **11**, 3742–3750.

22 R. Sharma, S. B. Simonsen, P. Morgen and S. M. Andersen, *Electrochim. Acta*, 2019, **321**, 134662.

23 R. Sharma, S. Gyergyek, P. Morgen and S. M. Andersen, *J. Electrochem. Soc.*, 2020, **167**, 024521.

24 R. Sharma, S. J. Andreasen, J. Chamier and S. M. Andersen, *J. Electrochem. Soc.*, 2019, **166**, F963.

25 F. Xu, S. Mu and M. Pan, *Int. J. Hydrogen Energy*, 2010, **35**, 2976–2979.

26 C. F. Nørgaard, S. N. Stamatin and E. M. Skou, *Int. J. Hydrogen Energy*, 2014, **39**, 17322–17326.

27 M. K. Jha, J.-c. Lee, M.-s. Kim, J. Jeong, B.-S. Kim and V. Kumar, *Hydrometallurgy*, 2013, **133**, 23–32.

28 N. Hodnik, C. Baldizzone, G. Polymeros, S. Geiger, J.-P. Grote, S. Cherevko, A. Mingers, A. Zeradjanin and K. J. J. Mayrhofer, *Nat. Commun.*, 2016, **7**, 13164.

29 B. C. Hagelüken, *Platinum Met. Rev.*, 2012, **56**, 29–35.

30 P. Jovanovič, N. Hodnik, F. Ruiz-Zepeda, I. Arčon, B. Jozinović, M. Zorko, M. Bele, M. Šala, V. S. Šelih, S. Hočevar and M. Gaberšček, *J. Am. Chem. Soc.*, 2017, **139**, 12837–12846.

31 S. Cherevko, T. Reier, A. R. Zeradjanin, Z. Pawolek, P. Strasser and K. J. J. Mayrhofer, *Electrochem. Commun.*, 2014, **48**, 81–85.

32 R. V. Mom, L. J. Falling, O. Kasian, G. Algara-Siller, D. Teschner, R. H. Crabtree, A. Knop-Gericke, K. J. J. Mayrhofer, J.-J. Velasco-Vélez and T. E. Jones, *ACS Catal.*, 2022, **12**, 5174–5184.

33 L. Moriau, K. Stojanovski, P. Jovanovič, D. Escalera-López, S. Cherevko and N. Hodnik, *RSC Adv.*, 2023, **13**, 7980–7987.

34 S.-W. Xu, J. Li, N. Zhang, W. Shen, Y. Zheng and P. Xi, *Chem. Commun.*, 2023, **59**, 9792–9802.

35 N. Li, S. S. Araya, X. Cui and S. K. Kær, *J. Power Sources*, 2020, **473**, 228617.

36 M. Chourashiya, R. Sharma and S. M. Andersen, *Anal. Chem.*, 2018, **90**, 14181–14187.

37 R. Sharma, M. A. Karlsen, P. Morgen, J. Chamier, D. B. Ravnsbæk and S. M. Andersen, *ACS Appl. Energy Mater.*, 2021, **4**, 2552–2562.

38 H. Yoo, K. Oh, Y.-R. Lee, K. Row, G. Lee and J. Choi, *Int. J. Hydrogen Energy*, 2017, **42**(10), 6657–6664.

39 P. Vanysek, *CRC handbook of chemistry and physics*, 2000, vol. 8, pp. 8-33.

40 V. Karimi, R. Sharma, P. Morgen and S. M. Andersen, *ACS Appl. Mater. Interfaces*, 2023, **15**, 49233–49245.

41 R. Kötz, in *Spectroscopic and Diffraction Techniques in Interfacial Electrochemistry*, ed. C. Gutiérrez and C. Melendres, Springer Netherlands, Dordrecht, 1990, pp. 409–438, DOI: 10.1007/978-94-011-3782-9_14.

42 Z. Pavlovic, C. Ranjan, Q. Gao, M. van Gastel and R. Schlögl, *ACS Catal.*, 2016, **6**, 8098–8105.

43 E. El Sawy and V. Birss, *J. Mater. Chem.*, 2009, **19**, 8244–8252.

44 J. Juodkazytė, B. Šebeka, I. Valsiûnas and K. Juodkazis, *Electroanalysis*, 2005, **17**, 947–952.

45 I. M. Tidswell, C. A. Lucas, N. M. Marković and P. N. Ross, *Phys. Rev. B: Condens. Matter Mater. Phys.*, 1995, **51**, 10205–10208.

46 C. L. Scortichnini and C. N. Reilley, *J. Electroanal. Chem. Interfacial Electrochem.*, 1982, **139**, 233–245.

47 N. M. Marković, C. A. Lucas, H. A. Gasteiger and P. N. Ross, *Surf. Sci.*, 1997, **372**, 239–254.

48 M. Palomar-Pardavé, I. González and N. Batina, *J. Phys. Chem. B*, 2000, **104**, 3545–3555.

49 J. Okada, J. Inukai and K. Itaya, *Phys. Chem. Chem. Phys.*, 2001, **3**, 3297–3302.

50 J. Mozota and B. Conway, *J. Electrochem. Soc.*, 1981, **128**, 2142.

51 N. Li and J. Lipkowski, *J. Electroanal. Chem.*, 2000, **491**, 95–102.

52 Z. Shi and J. Lipkowski, *J. Electroanal. Chem.*, 1996, **403**, 225–239.

53 D. M. Soares, S. Wasle, K. G. Weil and K. Doblhofer, *J. Electroanal. Chem.*, 2002, **532**, 353–358.

54 W. Shao, G. Pattanaik and G. Zangari, *J. Electrochem. Soc.*, 2007, **154**, D201.

55 D. J. Miller, M. C. Biesinger and N. S. McIntyre, *Surf. Interface Anal.*, 2002, **33**, 299–305.

56 S. Ben Jadi, A. El Guerraf, A. Kiss, A. El Azrak, E. A. Bazzaoui, R. Wang, J. I. Martins and M. Bazzaoui, *J. Solid State Electrochem.*, 2020, **24**, 1551–1565.

57 C. Chen, G. Levitin, D. W. Hess and T. F. Fuller, *J. Power Sources*, 2007, **169**, 288–295.

58 A. K. Friedman, W. Shi, Y. Losovyj, A. R. Siedle and L. A. Baker, *J. Electrochem. Soc.*, 2018, **165**, H733–H741.

59 R. Sharma, P. Morgen, M. J. Larsen, M. C. Roda-Serrat, P. B. Lund, L. Grahl-Madsen and S. M. Andersen, *ACS Appl. Mater. Interfaces*, 2023, **15**, 48705–48715.

60 R. Sharma, P. Morgen, S. Chiriaev, P. B. Lund, M. J. Larsen, B. Sieborg, L. Grahl-Madsen and S. M. Andersen, *ACS Appl. Mater. Interfaces*, 2022, **14**, 49658–49671.

61 M. Takasaki, Y. Nakagawa, Y. Sakiyama, K. Tanabe, K. Ookubo, N. Sato, T. Minamide, H. Nakayama and M. Hori, *ECS Trans.*, 2009, **17**, 439.

62 M. Robert, A. E. Kaddouri, J.-C. Perrin, S. Leclerc and O. Lottin, *J. Electrochem. Soc.*, 2018, **165**, F3209.

63 C. G. Chung, L. Kim, Y. W. Sung, J. Lee and J. S. Chung, *Int. J. Hydrogen Energy*, 2009, **34**, 8974–8981.

64 G. Gupta, S. Sharma and P. M. Mendes, *RSC Adv.*, 2016, **6**, 82635–82643.

65 V. Pfeifer, T. E. Jones, J. J. Velasco Vélez, C. Massué, R. Arrigo, D. Teschner, F. Girgsdies, M. Scherzer, M. T. Greiner, J. Allan, M. Hashagen, G. Weinberg, S. Piccinin, M. Hävecker, A. Knop-Gericke and R. Schlögl, *Surf. Interface Anal.*, 2016, **48**, 261–273.

66 M. N. Le and M. S. Lee, *Geosyst. Eng.*, 2018, **21**, 210–216.

67 U. Otgonbayar, L. Sandig-Predzymirska, A. Thiere and A. Charitos, *Hydrometallurgy*, 2024, **226**, 106303.

68 M. Fan, S. Li, H. Deng, X. Zhang, G. Luo, Z. Huang and M. Chen, *Sep. Purif. Technol.*, 2022, **289**, 120765.